# Supporting Information

## Smith et al. 10.1073/pnas.1211164110

### SI Materials and Methods

**Protein Purification and Labeling.** Actin was purified from rabbit muscle as described (1). To fluorescently label actin, it was first polymerized overnight at 4 °C in Pipes buffer [50 mM KCl, 0.1 mM $MgCl_2$, 0.2 mM ATP, 25 mM $K^+$-Pipes (pH 8.3)], reacted with Alexa Fluor 488 tetrafluorophenyl ester (AF488-TFPE; Molecular Probes) for 3 h at 22 °C, dialyzed against G-buffer [3 mM Tris·$Cl^-$, 0.1 mM $CaCl_2$, 0.2 mM ATP, 0.5 mM DTT (pH 8)] for 2 d at 4 °C to depolymerize, and gel filtered (1). To biotinate actin, the same procedure was followed, except that actin was reacted with maleimide-$PEG_2$-biotin (Pierce/Thermo Fisher).

Actin-related protein (Arp) 2/3-SNAP was purified from a *Saccharomyces cerevisiae* strain in which the *ARC18* locus was modified to produce an Arc18-SNAP fusion protein. To construct the strain expressing the Arc18 subunit with C-terminal SNAP tag, tobacco etch virus (TEV) protease site, and 3HA tags, we first used PCR to amplify the ARC18-TEV-3HA::HIS sequence from BGY694 (2), including 300 bases both upstream and downstream. The primers contained XhoI and NotI sites. This construct was subcloned into the XhoI/NotI sites of pRS305 (3). The SNAP tag sequence (pSET7-s6b; New England Biolabs) was amplified with two primers containing SmaI sites (5′-GCG CGC CCG GGA ATT CCA CCG GAT CCA CCA G-3′ and 5′-GCG CGC CCG GGG GAG GAT CTG GTG GTT CTG GAT CCA TGG ACA AAG ATT GCG AAA TG-3′) and cloned between ARC18 and TEV. The resulting ARC18-SNAP-TEV-3HA construct was liberated with an XhoI/NotI digest and transformed into BGY311 (4) to generate BGY1430.

BGY1430 cultures were grown and Arp2/3-SNAP was isolated as described (5). When desired, the SNAP tag was labeled during purification by incubating the Arp2/3-SNAP-TEV-3HA bound to α-HA antibody-coated Sepharose CL4B beads with SNAP-Surface 549 (New England Biolabs) for 2 h at 22 °C, then washing to remove free dye before TEV protease cleavage.

Full-length yeast WASp/Las17 (6) and its VCA domain (7) were purified as described. Chicken muscle CapZ was purified essentially as described (8).

**Actin Assembly Kinetics.** Bulk actin assembly assays were performed essentially as described (2) using 2 μM gel-filtered actin monomers (with 5% of monomers labeled with pyrenyl-iodoacetamide), Arp2/3 complex (10 or 20 nM), and Las17 (10 nM; Fig. 1*B*) or its VCA fragment (Fig. S2). Pyrene fluorescence was monitored at 0.3 Hz at excitation 365 nm and emission 407 nm in a fluorescence spectrophotometer (Photon Technology International). The assay was designed so that at its midpoint (1 μM) G-actin, it mimicked the conditions of the single-molecule measurements.

During the pyrene assay the G-actin concentration $G(t)$ decreases with time and the F-actin concentration $F(t)$ increases. To interpret the fluorescence records, we first assumed that the level at which the pyrene fluorescence signal plateaus corresponds to a steady-state F-actin concentration $F_{max}$ of 1.9 μM, and the G-actin critical concentration $G_o$ of 0.1 μM (9, 10). In contrast, at the start of the reaction $G(0)$ is 2 μM and $F(0)$ is zero. These initial and final values were used to scale the florescence records to yield the time course of F-actin concentration, $F(t)$.

Barbed-end concentrations $E(t)$ were calculated (11) from the rate of change of F-actin concentration as

$$E(t) = F'(t)/r_e(t),$$

where $F'(t)$ is the numerical derivative of the smoothed (10- to 20-point sliding-mean filter) $F(t)$, and $r_e(t)$ is the time-dependent rate of actin elongation calculated as

$$r_e(t) = r[G(t) - G_o] = r[F_{max} - F(t)],$$

where $r$ is 10 $s^{-1}\cdot\mu M^{-1}$, the elongation rate constant (9, 10).

To calculate the time-dependent branch concentration $B(t)$ from pyrene–actin curves, the concentration of barbed ends resulting specifically from branch formation was calculated as

$$B(t) = \left[F'_{+A}(t) - F'_{-A}(t)\right] \Big/ \{r[F_{max} - F_{+A}(t)]\},$$

where the subscripts +A and –A designate records collected in the presence and absence of Arp2/3 complex, respectively. Finally, the apparent second-order rate constant for branch production $k_B(t)$ was calculated as the time derivative of the branch concentration divided by the F-actin and Arp2/3 complex concentrations

$$k_B(t) = B'(t)/[F_{+A}(t)A] = \frac{1}{rF_{+A}(t)[F_{max} - F_{+A}(t)]A(t)} \left\{ [F_{+A}(t) - F_{-A}(t)]'' + \frac{[F_{+A}(t) - F_{-A}(t)]' F'_{+A}(t)}{F_{max} - F_{+A}(t)} \right\},$$

where $B'(t)$ is the numerical derivative of the smoothed (50-point sliding-mean filter) $B(t)$ . In this calculation, the concentration of free Arp2/3 complex, $A(t)$, was taken to be (20 nM) − $B(t)$. The branching rate-constant data were further smoothed by 50-point sliding-mean filter and expressed per unit length of filament by multiplying by the linear subunit density in F-actin, 360 $\mu m^{-1}$. The resulting branching rate time-courses (Fig. S2*C*) were uninterpretably noisy for $t < \sim 250$ s due to the low levels of F-actin present early in the reaction. The branching rate reached a comparatively stable plateau in the time interval $\sim 300$ s $< t < \sim 600$ s, and subsequently declined due to depletion of monomeric actin and/or depletion of free Arp2/3 complex by nonproductive filament binding. We calculated the mean branch formation rate-constant in the plateau region and found that this agreed within experimental uncertainty with total internal reflection fluorescence (TIRF) measurements of the branching rate for reactions both in the presence and absence of VCA (Fig. S2*D*).

**Microscope Flow Chambers.** Flow chambers of ~3 μL volume were constructed from a no. 1.5 cover glass-bottom (24 × 60 mm) and a glass microscope slide top (25 × 20 mm); both were cleaned by sonicating multiple times (1 h in detergent, 1 h ethanol, 30 min 0.1 M KOH, and 15 min deionized water) and then treated with 2 mg/mL methoxy-$PEG_{5000}$-silane (Laysan Bio) in 80% (vol/vol) ethanol (pH 2), 70 °C overnight. The reaction for the bottom

also contained 0.02 mg/mL biotin-$PEG_{3400}$-silane. Holes drilled in the chamber top were attached to reservoirs made from micropipette tips (for fluid inlet) or to polyethylene tubing (for fluid outlet) and sealed with epoxy. Top and bottom were assembled separated by 30-μm-thick double-sided acrylic/polyester adhesive strips (Nitto Denko) and sealed with epoxy. The fluid outlet was connected to a valve (Hamilton) and syringe pump (Harvard Apparatus) controlled by custom software. Fluid was introduced into the flow chambers at 20–60 μL/min. Before each experiment, flow chambers were coated for 15 min with buffer [5 mg/mL BSA, 50 mM KCl, 1 mM $MgCl_2$, 1 mM EGTA, 10 mM imidazole (pH 7.5)], then for 30 s with 0.05 mg/mL streptavidin in the same buffer. Next, the chamber was washed with 3 × 10 μL buffer and immediately loaded with preassembled filaments.

**TIRF Microscopy.** Dual-wavelength TIRF microscopy was performed on a custom-built microscope described previously (12). TIRF buffer contained 50 mM KCl, 1 mM $MgCl_2$, 1 mM EGTA, 10 mM imidazole (pH 7.5), 10 mM DTT, 0.2 mM ATP, 15 mM glucose, 0.02 mg/mL catalase, 0.1 mg/mL glucose oxidase, 0.1% BSA, and 0.25% methylcellulose.

To excite fluorescence from actin filaments and Arp2/3 complexes, lasers beams from solid-state 488-nm (Spectra-Physics) and 532-nm (CrystaLaser) lasers were directed in and out of the microscope objective with small broadband mirrors aligned to create an evanescent excitation field at the surface of the sample chamber (12). A third laser beam at 785 nm (Power Technology) reflected off the microscope slide and directed to a quadrant photodetector (Pacific Silicon Sensor) was used to stabilize focus through feedback to the piezoelectric microscope stage (13). Fluorescence emissions were collected on an electron-multiplying charge-coupled device (Andor).

Unless otherwise stated, TIRF experiments were conducted according to one of the following two protocols:

*i*) For branching experiments, filaments were preassembled for ~5 min with 3 μM actin (10% of monomers AF488 labeled, 1% biotinated) in TIRF buffer without methylcellulose, then diluted to 1.5 μM total actin with buffer containing methylcellulose and immediately injected into the flow chamber. Once short filaments were observed on the microscope slide surface, the assembly mixture was exchanged with TIRF buffer containing 1 μM monomeric actin (10% AF488 labeled, 1% biotinated) and 20 nM labeled Arp2/3 complex, with or without 300 nM VCA. Fluorescence images of Arp2/3 complex were acquired continuously with 532 nm excitation at 0.1 or 0.2 s per frame. Every 6–9 s, the 532-nm laser was shuttered, a single frame of actin fluorescence was recorded with 488 nm excitation, and the microscope was automatically refocused. These interruptions of the Arp2/3 complex recording took ~1 s.

*ii*) To maximize the time over which Arp2/3 complex binding to and dissociating from actin filaments could be observed without the microscope field of view becoming obscured by a dense network of filaments, an altered protocol was used. Filaments were preassembled as above except that only 5% of actin monomers were labeled with AF488, assembly was allowed to proceed for 1–2 h, and subsequent dilution was 40-fold (to ~75 nM F-actin) in TIRF buffer containing methylcellulose and 20 nM capping protein (CapZ). Once these long, capped filaments became tethered to the microscope slide, the solution was exchanged with buffer containing 1 μM monomeric actin (10% AF488 labeled, no biotin–actin), 10–20 nM CapZ, and 10 nM labeled Arp2/3 complex, with or without 300 nM VCA. Because the filaments were very stable under these conditions, Arp2/3 complex fluorescence was recorded continuously with only brief interruptions every 30–40 s to image actin (to confirm the continued presence of tethered filaments) and to autofocus.

**Image Analysis.** Image processing was performed with custom programs developed in LabVIEW (National Instruments) and in MatLab (MathWorks), and with ImageJ (National Institutes of Health). Further data analysis was performed in MatLab and Origin (OriginLab) software.

**TIRF Measurement of Branch Formation Rate.** Branch formation rates were measured from TIRF recordings by counting branches formed on a sample of mother filament segments. We selected segments (typically 2–20 μm in length) that were continuously visible for >10 min before being obscured by other filaments. For each segment $i$, which had length $L_i$, we counted the total number of branches, $n_i$, that appeared over the observation time $t_i$. The second-order branching rate constant was then calculated as

$$k_B = \frac{\sum_i n_i}{A_o \sum_i L_i t_i},$$

where $A_o$ is the initial Arp2/3 complex concentration, 20 nM.

To confirm that the microscope slide surface does not interfere with branch formation, we compared the linear density of branches on filaments polymerized on the surface (0.04 ± 0.01 $\mu m^{-1}$) with the branch density on filaments that first polymerized in solution above the surface and then settled into the TIRF field (0.07 ± 0.02 $\mu m^{-1}$). Taken together with the comparison of branch formation rates obtained from bulk actin assembly with those from TIRF recordings (Fig. S2*D*), this data showed that the slide surface causes little or no inhibition of Arp2/3 complex activation.

**Single Molecules of Arp2/3 Complex at Branch Sites.** Arp2/3 complex fluorescence intensity records (Fig. 3*A*, gray) were produced by integrating images over a 0.5- × 0.5-μm region centered at the branch site. To suppress noise, intensity records were filtered (Fig. 3*A*, green) with a five-frame sliding average. We observed that 90 ± 3% (143/160) of branch junctions displayed a spot of Arp2/3 complex fluorescence. In all cases, Arp2/3-SNAP549 complex fluorescence was observed to first appear in a single discrete step increase over background fluorescence, consistent with binding of a labeled Arp2/3 complex from the solution. In 97 ± 2% (112/116) of the records in which the spot was subsequently seen to disappear (presumably by photobleaching, because Arp2/3 complex remains irreversibly bound at branch junctions), the disappearance occurred in a single step, indicating that only a single fluorophore was present at the junction (Fig. S1*C*). These data are consistent with the hypothesis that branches were formed by a single Arp2/3 complex bound to the mother filament (with 90% having a fluorescent label) and inconsistent with hypotheses that dimers or higher-order aggregates of Arp2/3 complex are required (Fig. S1*E*). In a relatively small number of records (33/143), a second abrupt increase in Arp2/3 complex fluorescence was seen before the first spot had photobleached. Such events were assumed to arise from binding of a second Arp2/3 complex to the mother or daughter filament near the branch junction. These records were excluded from the photobleaching analysis, and they were also excluded from the activation time analyses if the second binding event happened before daughter filament nucleation (Fig. 3).

The fluorescent spots observed at branch sites had a wide range of intensities (Fig. 1*C*). This variation in intensity is likely due to different branch points being at different positions above the microscope slide surface and at different locations within the field of view, because the intensity of the excitation evanescent field varies steeply with distance above the slide surface and is somewhat inhomogeneous across the field. The distribution of

intensities of all fluorescent spots at branch sites together with the distribution of those that photobleached in a single step is shown in Fig. S1*D*. Both distributions have the same shape (single broad peak), consistent with the interpretation that branch sites are occupied by a single Arp2/3 complex.

**Activation Delay Times.** Activation times were measured by comparing the Arp2/3 complex fluorescence intensity records to daughter filament length records that were produced by manually tracing the filament contour. To improve accuracy, only daughter filaments whose elongation could be followed as they grew from ~0.3 to 1.5 μm were selected for analysis. Daughter length measurements between ~0.3 and 1.5 μm were fit with a linear function to obtain the nucleation event time (subject to the assumption that the polymerization rate is constant). The time of Arp2/3 complex binding to mother filament was identified as a step increase in the integrated fluorescence intensity at a nascent branch junction (Fig. 3*B*). The lag between Arp2/3 complex binding and daughter nucleation was defined as the activation delay time ($t_a$) for each branch. The measured $t_a$ values ranged from <0 to >20 s, but this variability was due in part to imprecision in measuring the lengths of short daughter filaments. For a precise measure of the characteristic activation time, $\langle t_a \rangle$, daughter length records were aligned based on the time at which each Arp2/3 complex bound the mother filament. For all branches observed in a given experiment, the time-length data were then binned according to length and the time values in each bin averaged to determine the mean time to reach the length corresponding to the mean of the length data in the bin (Fig. 3*B*, blue points). These combined data were linear fit with $1/SE^2$ weighting to obtain $\langle t_a \rangle$. The $\langle t_a \rangle$ values were averaged over three independent experiments.

To test for systematic errors in the measurements of daughter filament length, and therefore nucleation time, we generated simulated fluorescence image sequences of branch formation and elongation. The simulations were based on a mathematical model of the experiment that included (*i*) stochastic incorporation of labeled actin subunits into filaments; (*ii*) stochastic (Poisson-distributed) photon emissions from each dye; (*iii*) a 2-D Gaussian point-spread function; (*iv*) stochastic photobleaching; and (*v*) variable nucleation times, branching angles, and locations of the branch on the mother filament. To mimic the experimental data as closely as possible, these resulting idealized branch movies were summed with movies of measured background fluorescence. Analyzing these simulated recordings of branch nucleation and growth in the same way as the real data were analyzed yielded a difference between the measured and simulated nucleation time of 0.6 ± 1.8 s, demonstrating that there was no significant systematic error in the measurements, and that the estimated statistical uncertainty in the analysis was similar for the simulated and real experimental data. The simulations did not account for the possibility of pauses in daughter filament elongation, or for possible fluctuations of the daughter filament out of the field of TIRF illumination, both of which could influence the accuracy of the calculation of nucleation time.

**Arp2/3–Filament Binding Kinetics.** To quantify Arp2/3–filament binding and dissociation kinetics, we used automated identification and tracking of Arp2/3 complex fluorescent spots by an algorithm described previously (14). Before spot detection, Arp2/3 complex image sequences acquired at 0.1 or 0.2 s per frame were typically smoothed by a rolling average of the images such that the final temporal resolution was 0.5–1 s. Each filament path was traced in the actin fluorescence images to define the center line of a mask of width 0.7–0.9 μm used to select the subset of Arp2/3 complex spots that colocalized with filaments. For the background control, spots from background regions were selected the same way using a simulated filament path.

To find the rate constants for Arp2/3–filament bindings, we measured the initial binding rate of Arp2/3 complex to filament segments of fixed length. This analysis protocol was chosen because it minimizes effects from photobleaching or blinking of bound Arp2/3 complexes. Specifically, we treated filament segments of length $l_s = 0.4$ μm (approximately the spatial resolution of the microscope) as independent locations for Arp2/3 complex binding. The times to first Arp2/3 complex binding observed in each segment were fit with exponential probability distribution functions (Fig. S3). It is important to note that individual segments do not represent single binding sites, but contain many, possibly overlapping, sites where Arp2/3 complex can bind the filament. By restricting our analysis to the first binding event observed in each segment we avoid artifacts resulting from occupation of multiple unresolved sites in the segment and from photophysical blinking or bleaching of the dye label. The resulting apparent rate constants were converted to units of $M^{-1}{\cdot}s^{-1}{\cdot}\mu m^{-1}$ by dividing by the segment length ($l_s$) and by the total concentration of Arp2/3 complex in the reaction ($c_{Arp}$). In the fits, the fraction of filament segments available for binding Arp2/3 complex was treated as a free parameter, because some segments may have been blocked by interaction with the microscope slide surface. This fraction was 0.84 ± 0.09 (mean ± SE over three independent trials), suggesting that interference from the slide surface was minimal, but providing a possible explanation for the observed nonuniform distribution of Arp2/3 complex binding locations on filaments (Fig. 2*A*).

Nonspecific binding of Arp2/3 complex to the slide surface was measured by applying the same analysis method to regions in which no filaments were observed. These background control regions we segmented as above, and the times to first binding in each segment were recorded. Exponential fits to the distribution of these times produced the rate constant for slide binding per unit path length (analogous to filament length for the regions of the slide containing a filament). Corrected rate constants for binding of Arp2/3 complex to filaments were calculated as $k_{on} = (k_{fil} - k_{bkg})/n$, where $k_{fil}$ is the filament-region binding rate, $k_{bkg}$ is background-region binding rate (Fig. S3), and $n = 360\ \mu m^{-1}$ is the number of subunits per unit length of F-actin.

To illustrate the agreement between binding data and the binding curves predicted by the measured rate constants, we first plotted background-corrected binding data curves (e.g., Fig. 2*B*). These were calculated as $1 - S_{fil}(t)/S_{bkg}(t)$, where $S_{fil}(t)$ and $S_{bkg}(t)$ are the fraction of segments from filament and background regions, respectively, that were not yet bound by Arp2/3 complex at time $t$. We then plotted the predicted binding curves as $1 - \exp(-k_{on}\, t\, A_o\, n\, l_s)$, where $A_o$ is the initial Arp2/3 complex concentration, 10 or 20 nM.

Fitting of binding data were performed using a maximum-likelihood algorithm that accounted for event intervals missed because they were too short (< 0.5–1 s) or too long (>10–15 min). SEs were estimated by bootstrapping.

**Arp2/3–Filament Dissociation Kinetics.** To quantify Arp2/3–filament dissociation kinetics, distributions of Arp2/3 complex lifetimes on filament regions were first corrected for slide binding by subtracting the frequency of observed events of the same lifetimes on background regions. These curves were then fit with two- or three-exponential probability functions to find the time constants $\tau_i$ and corresponding relative amplitudes, or fractions, $a_i$, of the different components of the distribution of lifetimes of Arp2/3–filament complexes (Fig. S5). After establishing that the longest time-constant ($\tau_3$) from three-exponential fits of lifetime data were the same with and without VCA and was equal to the photobleaching time constant at branch sites, the three data sets were globally fit with the constraint that the long time-constants were equal ($\tau_3 = \tau_{3V}$), but letting the amplitudes and shorter time-constants vary independently for ±VCA data. The fit parameters were averaged for two independent trials and are presented in Table S1. Fitting and error analysis of dissociation data were performed using the same methods as for binding data.

To test whether a two-exponential probability function was sufficient to fit the lifetime distributions, we compared two- and three-exponential models using the Bayesian information criterion (BIC) (15), BIC = $\ln(L) - k/2\ln(n)$, where $L$ is the maximized likelihood, $k$ is the number of free fit parameters, and $n$ is the number of measurements. The strength of evidence for selecting one model over another is considered substantial when the difference in BIC is >1.1 (>3:1 odds), strong when the difference is >2.3 (>10:1 odds), very strong when the difference is >3.4 (>30:1 odds), and decisive when the difference is >4.6 (>100:1 odds) (16). Based on these criteria, the three-exponential model provided a decisively better fit to our lifetime distributions than the two-exponential model (Fig. S5*C*). Confidence interval envelopes, shown as shaded regions in Fig. 2*B* and Fig. 4*A*, were calculated by fitting 5,000 different equal-length resamplings (bootstraps) of the measured data set, sorting the fit values at each time point, and plotting the fifth and 95th percentile, representing the 90% CI. Errors on mean fit parameters (Table S1) were taken as the larger of (*i*) the mean of the errors calculated for each independent trial by bootstrapping (SD of the bootstrap parameter distributions) or (*ii*) the SE of results from independent trials.

**Global Fitting of Kinetic Models.** To determine the values of the rate and equilibrium constants in a given kinetic model that produced the best agreement with experimental observations, we derived a set of equations to calculate model-predicted values of all of the quantities measured in our experiments: amplitudes and time constants from lifetime distributions, binding rates, activation times, activation efficiencies, and overall stimulation of branch formation, with and without VCA. The set of derived equations for each model were used to globally fit the data by minimizing the total $\chi^2$ difference between the predicted values and the observed results. All modeling included a stable dead-end state of filament-bound Arp2/3 complex because of the presence of a small number of long-lived Arp2/3–filament complexes that did not produce branches (Fig. S4). For simplicity, the dead-end state was included by assuming that a small minority of Arp2/3 complexes ($f_{de}$) are defective in such a way that they bind filaments irreversibly and do not lead to branches. The rate of binding of these defective complexes to filaments was assumed to be the same as $k_1$ (Fig. 4*B*). Thus, the effective rate of formation of dead-end complexes was $k_{DE} = f_{de}\, k_1$. The observed lifetimes of both the dead-end complexes and the branch-forming complexes is limited by the photobleaching rate ($k_{pb}$), which was treated as an additional free parameter. All other model parameters are defined in the kinetic scheme (Fig. 4*B*; Fig. S6*A*; Table S3) for the model being fit.

The equations used to fit the data with the favored model shown in Fig. 4*B* (with the constraint that $k_{-1} < k_{-2}$) are as follows:

| Measured quantity | Equation (red indicates parameters affected by VCA) |
|---|---|
| Filament binding rate | $k_{on} = f_{de}k_1 + (1 - f_{de})(k_1 + K_{eq}k_2)/(1 + K_{eq})$ |
| Short lifetime fraction | $a_1 = (1 - f_{de})K_{eq}k_2k_{-2}/[k_{on}(1 + K_{eq})(k_{-2} + k_3)]$ |
| Short time-constant | $\tau_1 = 1/(k_{-2} + k_3 + k_{pb})$ |
| Intermediate lifetime fraction | $a_2 = (1 - f_{de})k_1/[k_{on}(1 + K_{eq})]$ |
| Intermediate time-constant | $\tau_2 = 1/(k_{-1} + k_{pb})$ |
| Long lifetime fraction | $a_3 = 1 - a_1 - a_2$ |
| Long time constant | $\tau_3 = 1/k_{pb}$ |
| Activation time delay | $\langle t_a \rangle = 1/(k_{-2} + k_3)$ |
| Activation efficiency | $f_B = (1 - f_{de})K_{eq}k_2k_3/[k_{on}(1 + K_{eq})(k_{-2} + k_3)]$ |
| Branch formation rate | $k_B = k_{on}f_B$. |

The model prediction of the fold-stimulation of $k_B$ by VCA was used as a prediction of the fold-stimulation of rate actin assembly measured by bulk pyrene–actin assays.

For the model of Fig. 4*B*, note that in the case where $k_{-2} >> k_3$ (as our fitting results predict; Table S2), the kinetic competition for escape from the $A_2F$ bound state is shifted toward dissociation (to state $A_2$ + F) over activation (to state B), such that the activation time is $\langle t_a \rangle \sim 1/k_{-2} \sim \tau_1$, and the activation efficiency is $f_B \sim k_3/k_{-2}$. Furthermore, because in this model VCA alters the activation rate $k_3$ and not the dissociation rate $k_{-2}$, it is apparent that $f_B$ is affected by VCA, whereas $\langle t_a \rangle$ is not, consistent with our observations.

In fitting the data with the Fig. 4*B* model, we found that the off-filament conformational equilibrium constant ($K_{eq}$) and the filament binding rate of the closed, branch capable state ($k_2$) could not be determined independently; only the product is well-determined and reported in Table S2. Therefore, the data are insufficient to distinguish effects on $K_{eq}$ from effects on $k_2$, and the decision about which is affected by VCA is arbitrary. We chose to have $K_{eq}$ and not $k_2$ vary with VCA because there is precedent in the literature for a VCA-dependent conformational equilibrium of Arp2/3 complex in the absence of actin filaments (17–20).

Quantitative goodness-of-fit statistical comparisons of different models was achieved by computing the relative Akaike information criterion (AIC; ref. 21) for each model, assuming the underlying errors are normally distributed, using the total $\chi^2$ and the number of free model parameters ($k$) as AIC = $-\chi^2/2 - k$ (Table S3). The strength of evidence for selecting one model over another is interpreted from the difference in AIC values, as described above for BIC.

**Construction and Testing of Kinetic Models.** Our multiple experimental measurements (Arp2/3–filament binding and dissociation kinetics, activation time, and efficiency) taken together revealed key aspects of the mechanism of VCA-stimulated actin branch formation by Arp2/3 complex. We sought to build a kinetic model of branch formation that could explain our empirical observations with a minimum number of adjustable parameters (i.e., rate and equilibrium constants). The logic that guided the development of the primary model (Fig. 4*B*) was as follows:

First, because the Arp2/3–filament complex lifetime distributions show three distinct components, the model must include a minimum of three filament-bound states (minimum of two different reversibly bound states and at least one that is bound irreversibly or at least remains bound for a time longer than the photobleaching time). Second, because the observed activation time is most similar to the shorter of the time constants identified in the lifetime distributions ($\langle t_a \rangle \sim \tau_1 \sim 2$ s), we proposed that activation occurs as a transition out of the most unstable filament-bound state, and that a second state with intermediate lifetime ($\tau_2 \sim 10$–$15$ s) is not on the pathway to branch formation. Consistent with independent observations that there are at least two conformations of Arp2/3 complex when it is not bound to filament (17–20), we proposed that the two reversibly bound states ($A_1F$ and $A_2F$ in Fig. 4*B*) are populated by capture of two different conformations of Arp2/3 complex ($A_1$ and $A_2$) from solution by mother filament (F). Furthermore, we assume that these two unbound states can interconvert on a time scale that is fast compared with filament binding. Therefore, the basic structure of the parallel class of models, shown in Table S3, dictates that the relative number of Arp2/3–filament complexes in the productive vs. nonproductive pathways is determined by the off-filament conformational equilibrium constant $K_{eq}$ and the ratio of binding rate constants $k_2/k_1$. In this class of models, only the $A_2F$ state can undergo activation (with rate $k_3$) to form the branch state (B).

The goals of the kinetic model analysis were (*i*) to find a minimal kinetic model of branch formation by Arp2/3 complex consistent with our data and (*ii*) to explore possible mechanisms by which

branch formation is regulated by VCA. Our data tell us that the presence of maximally activating levels of VCA produces a ~twofold stimulation of the rate of Arp2/3 complex binding to filaments ($k_{on}$) and a ~threefold stimulation of the efficiency with which Arp2/3–filament complexes form branches ($f_B$). Furthermore, these two effects combine to produce an overall four- to sevenfold effect of VCA on branch formation. We first attempted to explain these data with simple models in which VCA modulates only a single parameter. In the context of the parallel class of models, modulation of $K_{eq}$ is predicted to affect both the effective binding rate (if $k_1$ and $k_2$ are different) and the activation efficiency (by differentially populating states in the productive pathway over the nonproductive pathway). Consequently, modulation of $K_{eq}$ also is predicted to affect the fraction of short- vs. longer-lived Arp2/3–filament complexes. However, our observations showed little change in the relative amplitudes of the different components of the lifetime distributions with VCA (Table S1). Thus, parallel models in which VCA only affects $K_{eq}$ were unable to globally fit the data (Table S3) and were therefore rejected; the same was true for models of other classes in which only one parameter was modulated by VCA.

To find a minimal model that could describe the observed effects of VCA and be consistent with all our data, it was necessary to have VCA affect a minimum of two model parameters. We considered a variety of such models both from the parallel class and from two other classes (Table S3). This procedure led to the selection of the model shown in Fig. 4*B*, with $k_{-2} > k_{-1}$ (i.e., $A_2F$ less stable than $A_1F$) and with VCA stimulating branch formation by acting to bias the off-filament conformation equilibrium ($K_{eq}$) and the activation rate ($k_3$). The only other model considered that produced a satisfactory goodness-of-fit statistic was the similar but more complex box model shown on the last line of Table S3. We also considered a variety of sequential models that contain only a single pathway for Arp2/3 complex interaction with the mother filament. None of these models produced an acceptable agreement with the data (Table S3); the results of the best-fitting of these models are shown in Fig. S6.

The parallel and sequential models correspond to orthogonal mechanisms of regulation of Arp2/3 complex in which the conformational equilibrium occurs off-filament or on-filament, respectively. More complex mechanisms of Arp2/3 complex-mediated branch formation that combine aspects of our two basic models (e.g., the box class; Table S3) can also be consistent with our data; and such more-elaborate models may be required to fully explain regulation of Arp2/3 complex activity by cellular factors. We favor the parallel model over the box model based on parsimony, because the fit of these models to our data are statistically equivalent but the box model contains an additional free parameter. The models evaluated demonstrate that a comparatively simple model with only two parameters modulated by VCA is sufficient to explain our observations, whereas further simplified models with only one VCA-modulated parameter are not sufficient.

**Detailed Comparison with Previous Work.** Early biochemical studies of Arp2/3 complex reported an apparent actin-binding affinity of 2.3 ± 0.3 μM (22) for Arp2/3 complex from *Acanthamoeba*. These measurements were made by cosedimentation of Arp2/3 complex with preassembled filaments following a 15-min period of incubation in the absence of VCA. In our experiments, we see that a few percent of Arp2/3–filament complexes are very long-lived (lifetimes >2 min; limited by photobleaching in our measurements). These complexes, though rare, have a large effect on the apparent affinity and suggest that the system may not reach equilibrium over a 15-min reaction. Using our measured kinetics, we predict that 6% of Arp2/3 complexes would be bound by 2.3 μM of filament after 15 min in the absence of VCA. This value is ~eightfold lower than the ~50% measured earlier (22), but a difference of this magnitude is not unreasonable given the very different conditions (e.g., species of Arp2/3 complex, concentration of G-actin).

Previous reports of pyrene-labeled Arp2/3 complex dissociation from actin filaments indicated an off-rate of $10^{-4}$–$10^{-3}$ $s^{-1}$, suggesting that Arp2/3–filament complexes are extremely kinetically stable (23, 24). In contrast, we find that there are multiple species of Arp2/3-F-actin, and 90% of the complexes formed dissociate far more quickly, at a rate of 0.5 $s^{-1}$. Similarly, the same studies reported Arp2/3–filament binding rates of 10–100 $M^{-1}{\cdot}s^{-1}$, well below our results ($k_{on}$ = 1,000–4,000 $M^{-1}{\cdot}s^{-1}$). The earlier work used *Schizosaccharomyces pombe* Arp2/3 complex, in contrast to the *S. cerevisiae* protein used here. It is possible that the species difference accounts for the 100- to 1,000-fold faster kinetics we observe, but this seems unlikely given that the overall nucleation activity of Arp2/3 complex from the two organisms is similar (25, 26). We favor the alternative explanation that the fluorescence enhancement of the pyrene–Arp2/3 complex measured in the earlier studies is not caused by filament binding per se but by a slower or rarer conformational change in Arp2/3 complex that occurs after binding, perhaps one associated with activation. This interpretation would also account for why our results for the branch formation efficiency and for the rate of the limiting step in the activation pathway (1.3% and $k_3$ = 0.007 $s^{-1}$, respectively, in the presence of VCA) differ so substantially from the results implied by the pyrene–Arp2/3 fluorescence data (~100% efficiency and >0.15 $s^{-1}$ activation rate). Interestingly, our results are partially consistent with conclusions based on modeling bulk actin assembly kinetics alone (11), in that our activation rates agree (0.008 $s^{-1}$), but there are significant differences between our measurements and the modeled binding and dissociation rates, and thus in the inferred activation efficiency (~40%).

In contrast with earlier studies, our work directly observes binding of individual Arp2/3 complexes to mother filaments and the formation of daughter filaments from these individual Arp2/3 complexes. By doing so, we demonstrate that Arp2/3 complex interaction with F-actin is highly dynamic and inefficient, with the majority of binding events leading to rapid dissociation (0.5 $s^{-1}$) rather than branch formation. These results were largely unexpected from previous work and provide unique insight into the mechanism of activation and regulation.


1. Spudich JA, Watt S (1971) The regulation of rabbit skeletal muscle contraction. I. Biochemical studies of the interaction of the tropomyosin-troponin complex with actin and the proteolytic fragments of myosin. *J Biol Chem* 246(15):4866–4871.
2. D'Agostino JL, Goode BL (2005) Dissection of Arp2/3 complex actin nucleation mechanism and distinct roles for its nucleation-promoting factors in *Saccharomyces cerevisiae*. *Genetics* 171(1):35–47.
3. Sikorski RS, Hieter P (1989) A system of shuttle vectors and yeast host strains designed for efficient manipulation of DNA in *Saccharomyces cerevisiae*. *Genetics* 122(1):19–27.
4. Hildebrand M, et al. (1991) Oral iloprost in healthy volunteers. *Eicosanoids* 4(3): 149–154.
5. Daugherty KM, Goode BL (2008) Functional surfaces on the p35/ARPC2 subunit of Arp2/3 complex required for cell growth, actin nucleation, and endocytosis. *J Biol Chem* 283(24):16950–16959.
6. Rodal AA, Manning AL, Goode BL, Drubin DG (2003) Negative regulation of yeast WASp by two SH3 domain-containing proteins. *Curr Biol* 13(12):1000–1008.
7. Winter D, Lechler T, Li R (1999) Activation of the yeast Arp2/3 complex by Bee1p, a WASP-family protein. *Curr Biol* 9(9):501–504.
8. Soeno Y, Abe H, Kimura S, Maruyama K, Obinata T (1998) Generation of functional beta-actinin (CapZ) in an *E. coli* expression system. *J Muscle Res Cell Motil* 19(6):639–646.
9. Pollard TD (1986) Rate constants for the reactions of ATP- and ADP-actin with the ends of actin filaments. *J Cell Biol* 103(6 Pt 2):2747–2754.
10. Kuhn JR, Pollard TD (2005) Real-time measurements of actin filament polymerization by total internal reflection fluorescence microscopy. *Biophys J* 88(2):1387–1402.
11. Zalevsky J, Lempert L, Kranitz H, Mullins RD (2001) Different WASP family proteins stimulate different Arp2/3 complex-dependent actin-nucleating activities. *Curr Biol* 11(24):1903–1913.

12. Friedman LJ, Chung J, Gelles J (2006) Viewing dynamic assembly of molecular complexes by multi-wavelength single-molecule fluorescence. *Biophys J* 91(3): 1023–1031.
13. Crawford DJ, Hoskins AA, Friedman LJ, Gelles J, Moore MJ (2008) Visualizing the splicing of single pre-mRNA molecules in whole cell extract. *RNA* 14(1):170–179.
14. Crocker JC, Grier DG (1996) Methods of digital video microscopy for colloidal studies. *J Colloid Interface Sci* 179:298–310.
15. Schwarz G (1978) Estimating the dimension of a model. *Ann Stat* 6(2):461–464.
16. Jeffreys H (1998) *The Theory of Probability* (Oxford Univ Press, London).
17. Goley ED, Rodenbusch SE, Martin AC, Welch MD (2004) Critical conformational changes in the Arp2/3 complex are induced by nucleotide and nucleation promoting factor. *Mol Cell* 16(2):269–279.
18. Rodal AA, et al. (2005) Conformational changes in the Arp2/3 complex leading to actin nucleation. *Nat Struct Mol Biol* 12(1):26–31.
19. Martin AC, et al. (2005) Effects of Arp2 and Arp3 nucleotide-binding pocket mutations on Arp2/3 complex function. *J Cell Biol* 168(2):315–328.
20. Xu X-P, et al. (2012) Three-dimensional reconstructions of Arp2/3 complex with bound nucleation promoting factors. *EMBO J* 31(1):236–247.
21. Akaike H (1974) A new look at the statistical model identification. *IEEE Trans Automat Contr* 19:716–723.
22. Mullins RD, Stafford WF, Pollard TD (1997) Structure, subunit topology, and actin-binding activity of the Arp2/3 complex from *Acanthamoeba*. *J Cell Biol* 136(2):331–343.
23. Beltzner CC, Pollard TD (2008) Pathway of actin filament branch formation by Arp2/3 complex. *J Biol Chem* 283(11):7135–7144.
24. Ti S-C, Jurgenson CT, Nolen BJ, Pollard TD (2011) Structural and biochemical characterization of two binding sites for nucleation-promoting factor WASp-VCA on Arp2/3 complex. *Proc Natl Acad Sci USA* 108(33):E463–E471.
25. Goode BL, Rodal AA, Barnes G, Drubin DG (2001) Activation of the Arp2/3 complex by the actin filament binding protein Abp1p. *J Cell Biol* 153(3):627–634.
26. Ti S-C, Pollard TD (2011) Purification of actin from fission yeast *Schizosaccharomyces pombe* and characterization of functional differences from muscle actin. *J Biol Chem* 286(7):5784–5792.

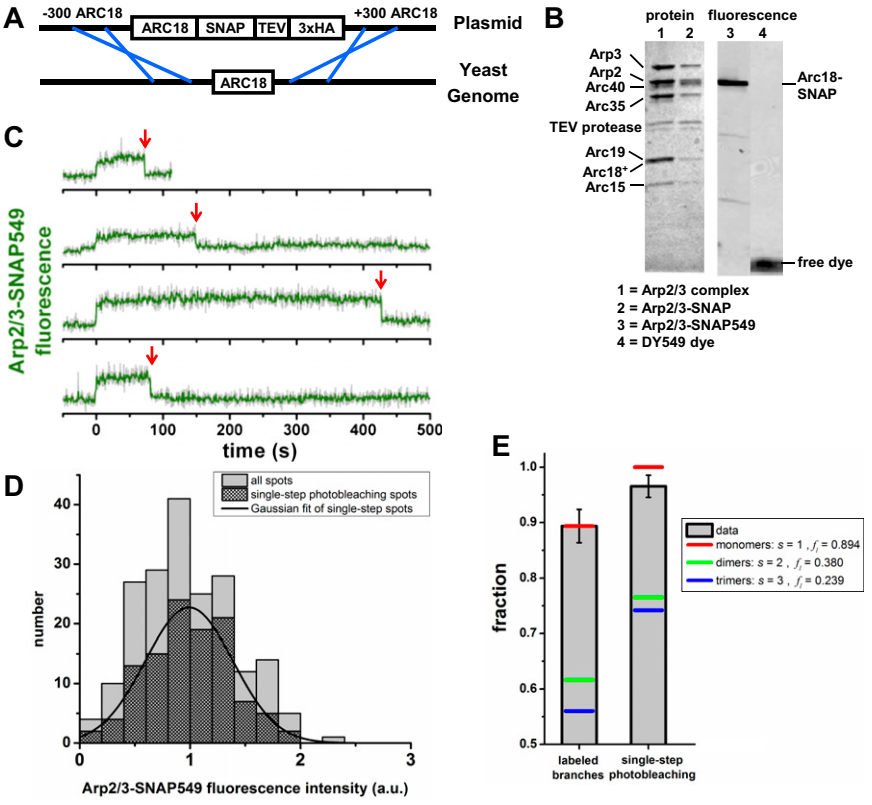


**Fig. S1.** Fluorescent labeling of Arp2/3 complex was subunit-specific and allowed visualization of single complexes at branch sites. (*A*) Strategy for tagging and fluorescent labeling of Arp2/3 complex. A DNA construct containing the Arc18/ARPC3 coding sequence fused at its C terminus to a SNAP tag, TEV protease cleavage site, and 3× HA epitope tag was integrated into the yeast genome via homologous recombination, replacing the endogenous *Arc18* locus. (*B*) Denaturing gel electrophoresis of purified Arp2/3 complex, Arp2/3-SNAP, and Arp2/3-SNAP549 complex. Protein stain (*Left*) and fluorescence scan (*Right*) revealed that the Arc18-SNAP subunit comigrated with Arp2 and Arc40, was specifically labeled, and that the labeled sample had negligible unreacted dye remaining after purification. Images are of nonadjacent lanes taken from the same gel. (*C*) Arp2/3 complex fluorescence records at four sites of branch formation; time 0 is defined as the time at which each spot of Arp2/3 complex fluorescence appeared. In all cases, the spot photobleached in a single step (arrows), but the branch remained after spot disappearance. (*D*) Test to examine whether the distribution of Arp2/3 complex fluorescence intensities is consistent with single fluorophores. Histograms of intensities of all fluorescent spots at branch sites ($n = 143$) compared with those that photobleached in a single step ($N_1 = 112$). (*E*) The fraction of branch junctions that display a spot of Arp2/3 complex fluorescent spots and the fraction of those spots that show single-step photobleaching (bars), with the corresponding best-fit predictions calculated assuming different Arp2/3 complex stoichiometries ($s$) at the branch junctions (lines). The fit results were found by varying the Arp2/3 complex-labeling fraction ($f_l$) and by using the binomial distribution to calculate the branch-labeling fraction as $1 - P_o$ and the single-step photobleaching fraction as $P_1/(1 - P_o)$, where $P_o = (1 - f_l)^s$ and $P_1 = s\, f_l(1 - f_l)^{s-1}$.

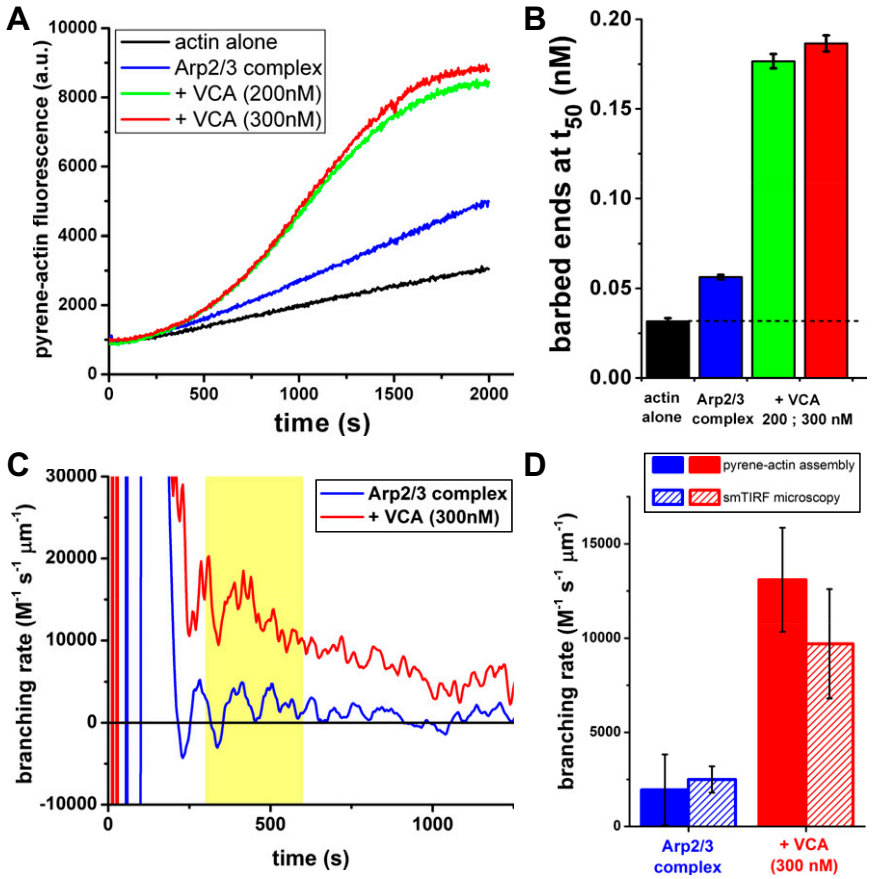


**Fig. S2.** VCA stimulated by sixfold the production of filament barbed ends by Arp2/3 complex. (*A*) Assembly of 2 μM actin (5% pyrene labeled) in the presence or absence of 20 nM Arp2/3 complex with or without the indicated concentrations of the VCA domain of yeast WASp. (*B*) Concentrations of filament barbed ends formed at 50% maximal assembly (±SE), calculated from the rate of pyrene–actin fluorescence increase (from fits to curves in *A*; *Materials and Methods*) shows that Arp2/3 complex activity is stimulated 6.3- ± 0.8-fold by VCA, after correcting for filaments generated by actin alone (dashed line) at a concentration of VCA (300 nM) that gives near-maximal stimulation. (*C*) Second-order branching rate constant over the course of the actin assembly reactions shown as red and blue traces in *A*, calculated directly from the second derivative of the increase in pyrene–actin fluorescence (*SI Materials and Methods*). (*D*) Branching rates calculated from pyrene–actin assembly assays in *C* (mean ± SD of the yellow plateau region) compared with branching rates measured by single-molecule TIRF microscopy (Fig. 1*C*).

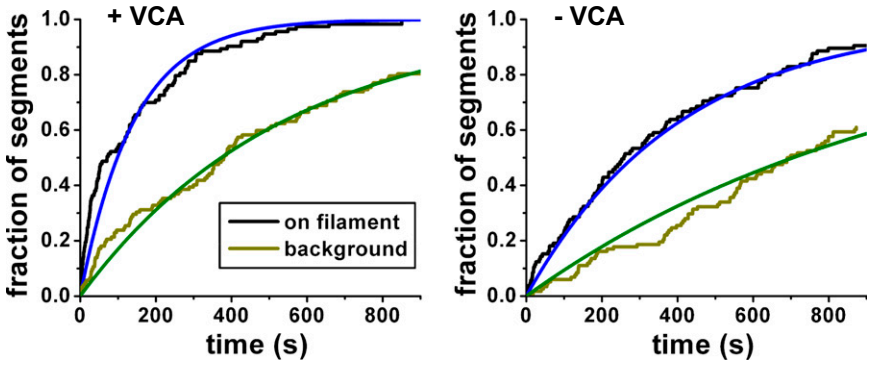


**Fig. S3.** Binding kinetics of 10 nM Arp2/3 complex to regions of the microscope slide where filaments were tethered and to "background" regions where no filaments were visible, in the presence of 1 μM actin and the presence or absence of 300 nM VCA. Plotted are the fractions of filament segments (0.4 μm in length) or equally sized segments of background regions, where at least one Arp2/3 complex was detected at or before the indicated observation times (*Materials and Methods*). Fits to data yielded apparent second-order binding rate constants (±SE): $k_{fil}$ = 1.7 ± 0.2 (+VCA) and 0.6 ± 0.1 (−VCA) × $10^6$ $M^{-1}{\cdot}s^{-1}{\cdot}\mu m^{-1}$ for binding filament regions, blue; $k_{bkg}$ = 0.5 ± 0.1 (+VCA) and 0.2 ± 0.1 (−VCA) × $10^6$ $M^{-1}{\cdot}s^{-1}{\cdot}\mu m^{-1}$ for binding background regions, green; the corresponding exponential probability distributions are displayed as solid lines. Data are from the experiment shown in Fig. 2*B*.

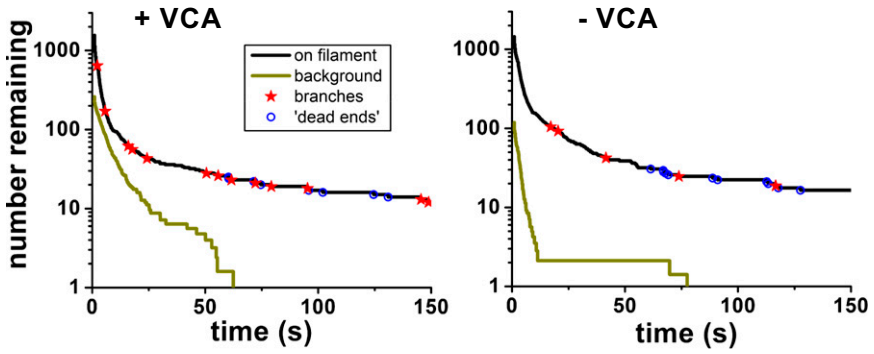


**Fig. S4.** Cumulative lifetime distributions of Arp2/3-SNAP549 fluorescent spots observed in filament-containing regions of the slide surface (~20-min observations of regions with total lengths of 237 μm with VCA and 195 μm without VCA, and widths of 0.7 μm) and those observed over equal times and areas in background regions that contain no detectable filaments. Plots show the number of spots with lifetimes less than or equal to the value indicated, observed in the presence or absence of VCA. Lifetimes of the Arp2/3–filament complexes that successfully nucleated daughter filaments (red stars) were used to assess the photobleaching rate of the Arp2/3-SNAP549 adduct. A small number (<0.5%) of spots had long lifetimes (>60 s) but did not produce visible daughter filaments (blue circles); these dead-end complexes may arise from incomplete assembly of or photodamage to a small fraction of Arp2/3 complexes.

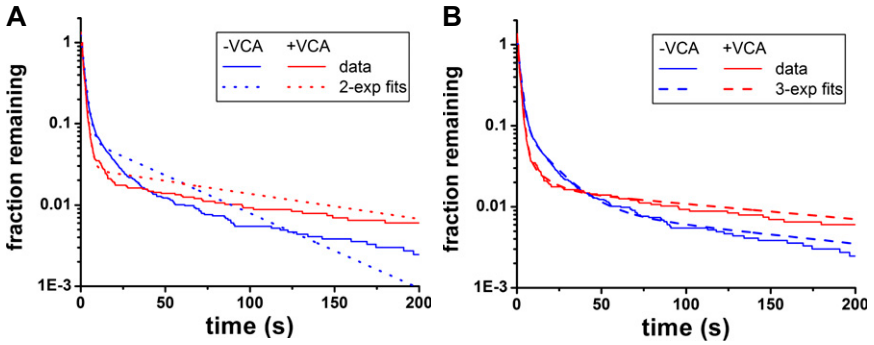


C

| | 2-exp fits | | 3-exp fits | |
|---|---|---|---|---|
| | -VCA | +VCA | -VCA | +VCA |
| $a_1$ | 0.947 ± 0.006 | 0.979 ± 0.003 | 0.915 ± 0.009 | 0.960 ± 0.008 |
| $\tau_1$ (s) | 2.04 ± 0.05 | 1.69 ± 0.05 | 1.88 ± 0.04 | 1.59 ± 0.04 |
| $a_2$ | 0.053 ± 0.006 | 0.021 ± 0.003 | 0.077 ± 0.008 | 0.028 ± 0.007 |
| $\tau_2$ (s) | 47 ± 9 | 140 ± 40 | 15 ± 2 | 10 ± 3 |
| $a_3$ | | | 0.008 ± 0.002 | 0.012 ± 0.003 |
| $\tau_3$ (s) | | | 190 ± 80 | 240 ± 80 |
| $\Delta BIC = BIC_{3exp} - BIC_{2exp}$ | | | 66 | 14 |

**Fig. S5.** There are more than two states of the Arp2/3–filament complex. (*A*) Fits using a two-exponential (exp) survival probability function failed to reproduce features of Arp2/3–filament lifetime distributions measured both with and without VCA. (*B*) A three-exponential function yielded better fits. (*C*) The fit parameters. Amplitudes were normalized, $\sum a_i = 1$; thus, the number of free parameters was three (2-exp) and five (3-exp). BIC statistical tests indicate that the three-exponential fits are decisively better than the two-exponential because ΔBIC >5 (*Materials and Methods*).

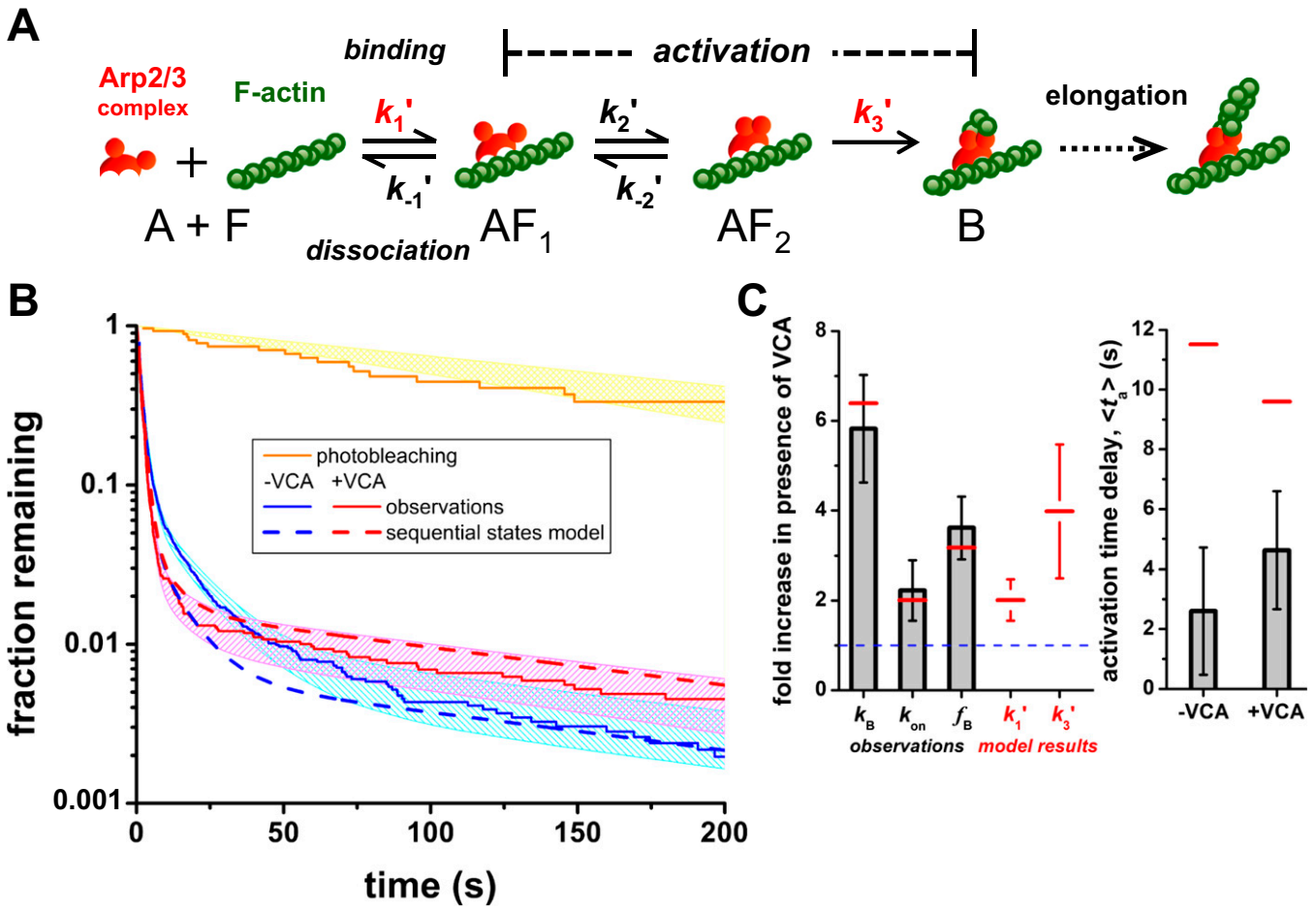


**Fig. S6.** Sequential model for Arp2/3 complex activation that fits experimental data less well than the model presented in Fig. 4*B*. (*A*) Kinetic scheme. Reversible binding of Arp2/3 complex to mother filament (producing state $AF_1$) is followed by activation through on-filament conformational changes leading to branch formation (state B) through the intermediate $AF_2$. Rate constants $k_1'$ and $k_3'$ (red) were allowed to assume different values in the presence and absence of VCA. (*B*) Example lifetime distributions of Arp2/3 complex on F-actin, with and without VCA (same data as in Fig. 4*A*), shown with fits using the sequential model. (*C*) Comparison of observed quantities (gray) and predictions from the model in *A* (red). VCA stimulation ratios (*Left*) of the rate of branch formation ($k_B$), the rate of Arp2/3 complex binding to filaments ($k_{on}$), and the fraction of filament-bound Arp2/3 complexes that nucleate daughter filaments ($f_B$) are shown together with the values of the two model parameters $k_1'$ and $k_3'$ that are VCA dependent. Also shown (*Right*) are the observed activation times and the corresponding model predictions, demonstrating that the model is inconsistent with the observations. The model in Fig. 4*B* is strongly favored over this sequential model ($\Delta$AIC = 3.4; Table S3).

**Table S1. Comparison of measurements to predictions of two kinetic models for the process of actin branch formation by Arp2/3 complex**

| | Observed mean ± SE | Parallel model, Fig. 4*B* | Sequential model, Fig. S6*A* |
|---|---|---|---|
| Binding rate per F-actin, three independent trials | | | |
| $k_{on}$, $M^{-1}{\cdot}s^{-1}$ | 1,400 ± 300 | 1,450 | 1,450 |
| $k_{onV}$, $M^{-1}{\cdot}s^{-1}$ | 3,000 ± 700 | 2,900 | 2,910 |
| Activation efficiency, three Independent trials | | | |
| $f_B$ | 0.004 ± 0.002 | 0.0043 | 0.0044 |
| $f_{BV}$ | 0.013 ± 0.004 | 0.0132 | 0.0140 |
| Activation delay, three independent trials | | | |
| $<t_a>$, s | 3 ± 2 | 2.1 | 11.5* |
| $<t_a>_V$, s | 5 ± 2 | 2.1 | 9.6* |
| Arp2/3–filament lifetime distributions, two independent trials with $n$ = (3,654, 3,694) and $N_V$ = (2,151, 1,335) observations | | | |
| $a_1$ | 0.91 ± 0.06 | 0.905 | 0.906 |
| $a_{1V}$ | 0.89 ± 0.07 | 0.941 | 0.903 |
| $\tau_1$, s | 2.1 ± 0.2 | 2.08 | 1.97 |
| $\tau_{1V}$, s | 1.9 ± 0.3 | 2.06 | 1.97 |
| $a_2$ | 0.08 ± 0.01 | 0.078 | 0.077 |
| $a_{2V}$ | 0.08 ± 0.05 | 0.039 | 0.070 |
| $\tau_2$, s | 15 ± 2 | 13.1 | 9.0 |
| $\tau_{2V}$, s | 11 ± 2 | 13.1 | 7.2 |
| $a_3$ (= 1 − $a_1$ − $a_2$) | 0.016 ± 0.008 | 0.017 | 0.017 |
| $a_{3V}$ (= 1 − $a_{1V}$ − $a_{2V}$) | 0.03 ± 0.02 | 0.020 | 0.027 |
| $\tau_3$, s | 140 ± 60 | 136 | 155 |

Values reported with and without VCA present are shown in red and blue, respectively.
*The sequential model fails to predict a short activation delay.

**Table S2. Parallel model, Fig. 4*B*: Values of the model parameters determined from fits to binding, dissociation, activation efficiency, and activation delay data**

| Model parameter | Fit value |
|---|---|
| $K_{eq}$ $k_2$, $M^{-1}{\cdot}s^{-1}$ | 1,500 ± 300 |
| $K_{eqV}$ $k_2$, $M^{-1}{\cdot}s^{-1}$ | 3,200 ± 600 |
| $k_1$, $M^{-1}{\cdot}s^{-1}$ | 130 ± 30 |
| $k_{-1}$, $s^{-1}$ | 0.07 ± 0.01 |
| $k_{-2}$, $s^{-1}$ | 0.47 ± 0.04 |
| $k_3$, $s^{-1}$ | 0.0022 ± 0.0005 |
| $k_{3V}$, $s^{-1}$ | 0.007 ± 0.001 |
| $k_{DE}$, $M^{-1}{\cdot}s^{-1}$ | 19 ± 9 |

Only the product of the rate constant $k_2$ and the equilibrium constant $K_{eq}$ are well-determined, not their individual values (although $k_2 >> k_1$). The effective rate of formation of dead-end complexes is indicated as $k_{DE}$. VCA-dependent parameters are shown in blue (–VCA) and red (+VCA). Means ± SE.

**Table S3. Comparison of kinetic models of branch formation**

| Type of model | Conditions | VCA-dependent parameters | Complexity* | Fitting results: ΔAIC† | Fitting results: Notes |
|---|---|---|---|---|---|
| 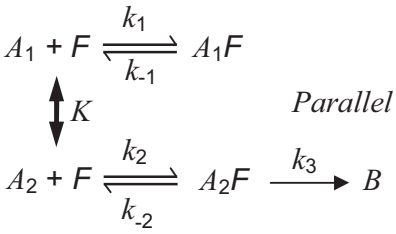 | $k_{-1} > k_{-2}$ | $K_{eq}$ | 7 | –10.6 | ¶ and § |
| | $k_{-1} > k_{-2}$ | $K_{eq}$, $k_{-2}$ | 8 | –11.1 | ¶ and § |
| | $k_{-1} > k_{-2}$ | $K_{eq}$, $k_3$ | 8 | –1.9 | § |
| | $k_{-1} > k_{-2}$ | $K_{eq}$ | 7 | –3.5 | ¶ |
| | $k_{-1} > k_{-2}$ | $K_{eq}$, $k_{-2}$ | 8 | –3.3 | ¶ |
| Parallel | $k_{-1} < k_{-2}$ | $K_{eq}$, $k_3$ | 8 | **0** | Fig. 4; Tables S1 and S2 |
| 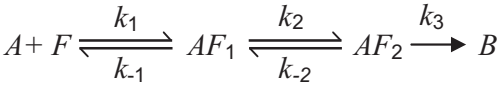 | | $k_1'$, $k_{-1}'$ | 7 | –9.0 | ¶ and § |
| | | $k_1'$, $k_{-2}'$ | 7 | –9.0 | ¶ and § |
| | | $k_1'$, $k_2'$ | 7 | –6.0 | § |
| Sequential | | $k_1'$, $k_3'$ | 7 | –3.5 | §; Fig. S6; Table S1 |
| 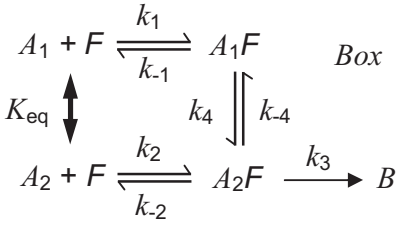 | $k_{-1} > k_{-2}$ | $K_{eq}$ | 8 | –11.0 | ‡, ¶, and § |
| | $k_{-1} > k_{-2}$ | $K_{eq}$, $k_4$ | 9 | –13.3 | ‡, ¶, and § |
| | $k_{-1} > k_{-2}$ | $K_{eq}$, $k_3$ | 9 | –4.0 | § |
| | $k_{-1} > k_{-2}$ | $K_{eq}$ | 8 | –4.7 | ¶ |
| | $k_{-1} > k_{-2}$ | $K_{eq}$, $k_4$ | 9 | –4.7 | ¶ |
| Box | $k_{-1} < k_{-2}$ | $K_{eq}$, $k_3$ | 9 | **–1.0** | |

*Number of fit parameters, excluding photobleaching rate and dead-end complex formation rate.
†The AIC (21) for a model is based on the goodness of fit ($-\chi^2$) with a penalty for increasing the number of free-model parameters ($k$): AIC = $-\chi^2/2 - k$. ΔAIC was calculated relative to the AIC for the favored model (parallel with $k_{-1} < k_{-2}$, with $K_{eq}$ and $k_3$ VCA dependent). No statistical preference for one model over another is indicated if the magnitude of ΔAIC is <1.1 (bold).
‡Predicted binding rate ($k_{on}$) does not increase with VCA enough to match observations.
¶Predicted activation efficiency ($f_B$) does not increase with VCA enough to match observations.
§Predicted activation delay is significantly longer ($\langle t_a \rangle \sim 10$ s) than the observed delays.

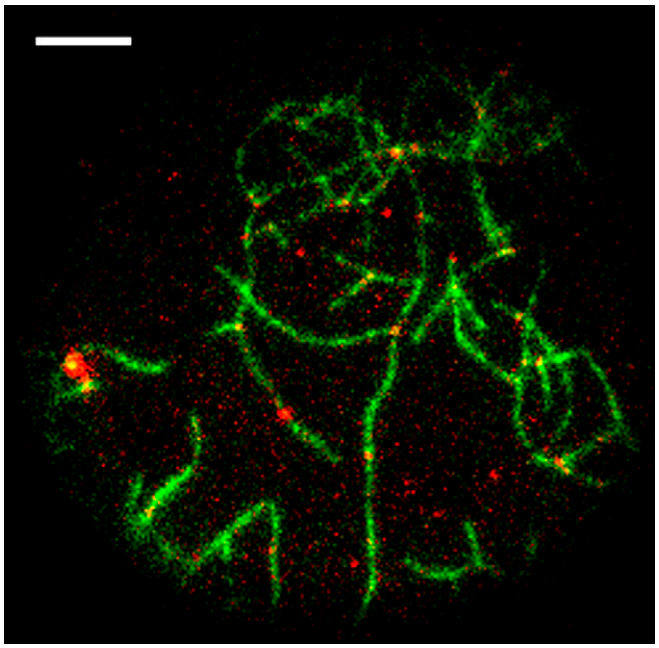

**Movie S1.** The dynamics of branched actin network assembly by Arp2/3 complex, corresponding to images shown in Fig. 1*C*. Dual-color TIRF microscopy merged image sequence of assembly of actin (green; 1 μM, 10% AF488-labeled, 1% biotin-labeled) in the presence of Arp2/3-SNAP549 (red; 20 nM) and VCA (300 nM, unlabeled). Actin images are single frames from time-lapse recordings (0.2-s duration every 6 s), whereas in this movie each Arp2/3 complex image was an average of five frames before and five frames (0.2 s per frame) following each actin frame. Playback is accelerated 50-fold. (Scale bar: 5 μm.)

Movie S1

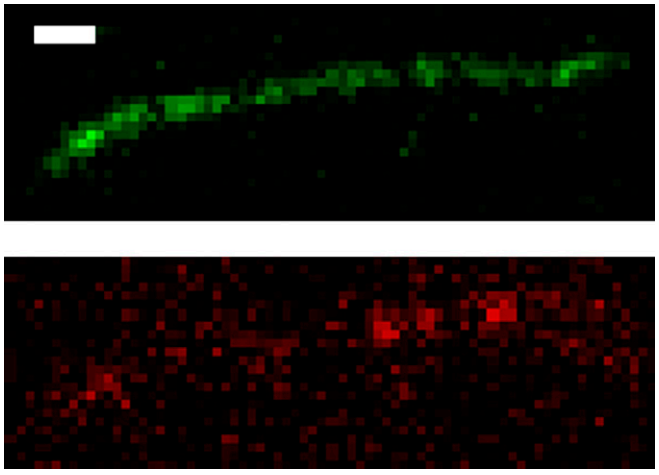

**Movie S2.** Arp2/3 complexes bound to F-actin display a broad range of lifetimes. Dual-color TIRF microscopy image sequence of Arp2/3-SNAP549 (red; 10 nM, continuous acquisition of 0.2-s duration images) binding and dissociating from stabilized actin filaments (green; 0.2-s duration images acquired once every 40 s) in the presence of 300 nM VCA, 1 μM monomeric actin (10% AF488-labeled), and 20 nM CapZ. Playback accelerated 10-fold. (Scale bar: 1 μm.)

Movie S2